Scale-by-scale non-equilibrium with Kolmogorov-like scalings in non-homogeneous stationary turbulence - Supplementary Material

P. Beaumard [1], P. Bragança [1], C. Cuvier [1], K. Steiros [2] and J.C Vassilicos [1] †

[1]Univ. Lille, CNRS, ONERA, Arts et Metiers Institute of Technology, Centrale Lille, UMR 9014 - LMFL - Laboratoire de Mécanique des Fluides de Lille - Kampé de Fériet, F-59000 Lille, France

[2]Department of Aeronautics, Imperial College London, London SW7 2AZ, United Kingdom

(Received 13 June 2023; revised 19 January 2024; accepted 24 February 2024)

In the present document, we provide supplementary information about the methods used to process the experimental data of the main publication and additional tests to check the robustness of the results.

1. Computation of the turbulence parameters

The following conventions are used to compute the different turbulent parameters.

1.1. *Dissipation*

The axisymmetric dissipation formulation is used (George & Hussein (1991)) where the rotation axis is z:

$$< \overline{\epsilon'} >= \nu < \overline{\left(-\left(\frac{\partial u_z'}{\partial z}\right)^2 + 2\left(\frac{\partial u_z'}{\partial x}\right)^2 + 2\left(\frac{\partial u_x'}{\partial z}\right)^2 + 8\left(\frac{\partial u_x'}{\partial x}\right)^2 \right)} >. \tag{1.1}$$

The dissipation is averaged both in space and time to obtain a converged estimate over the field of view. The notation $< . >$ is used for space averaging and $\overline{(.)}$ for time averaging.

Different estimates are tested to check the results' robustness with respect to the choice estimate. One of them is defined as:

$$< \overline{\epsilon'_\tau} >= \frac{\nu}{3} \overline{< \left(2 \times 15 \left(\frac{\partial u_x'}{\partial x}\right)^2 + 15 \left(\frac{\partial u_z'}{\partial z}\right)^2 \right) >} \tag{1.2}$$

and is evaluated in table 1 after signal denoising (method explained in the next paragraph). The results are different by less than 10% but more importantly the evolution from one configuration to the other is consistent. Therefore, the results' variation does not seems to be significantly dependent on the estimate choice so that dissipation scalings can be evaluated accurately. However, the value itself might contains some uncertainty.

The dissipation computation from experimental data is difficult because PIV introduces random noise during measurements. This noise significantly contaminates the dissipation (Foucaut *et al.* (2021)). Indeed, the turbulent energy is small at small scales so that noise can dominate at these scales. In the paper mentioned, the product of the derivatives used to compute dissipation is overestimated by 70% before denoising. The best way to denoise dissipation is to perform the experiment with two different PIV set-ups so that the noise of both measurements are decorrelated. The product of the derivatives obtained from the two systems cancel the random noise contribution (equation 1.3). Indeed, the noise is not correlated

† Email address for correspondence: john-christos.vassilicos@cnrs.fr

with the true signal and the noise of the two set-ups is decorrelated so it cancels out once averaged.

$$
\begin{aligned}
&< \frac{\partial u'}{\partial x}|_{s1} \times \frac{\partial u'}{\partial x}|_{s2} > \\
&=< \widehat{\frac{\partial u'}{\partial x}}|_{s1} \times \widehat{\frac{\partial u'}{\partial x}}|_{s2} > + < \beta_{s1} \times \widehat{\frac{\partial u'}{\partial x}}|_{s2} > + < \widehat{\frac{\partial u'}{\partial x}}|_{s1} \times \beta_{s2} > + < \beta_{s1} \times \beta_{s2} > \\
&=< \widehat{\frac{\partial u'}{\partial x}}|_{s1} \times \widehat{\frac{\partial u}{\partial x}}|_{s2} >
\end{aligned}
\tag{1.3}
$$

where $< . >$ is used for realization averaging here, s_1 (resp. s_2) refers to system 1 (resp. system 2), β is the random PIV noise and $\widehat{(.)}$ refers to denoised data (i.e. without noise but with PIV interrogation window filtering effect).

This double measurement was not possible for this experiment because of practical limitations. Therefore, a simplified denoising method is used. The idea is to use the measurement's high resolution (in space or in time) and shift the two derivatives by a small offset. This method introduces a small filtering of the true signal but the noise cancels out. The experimental measurements are highly resolved in time so time denoising is used:

$$
\begin{aligned}
&< \frac{\partial u'}{\partial x}|_{t} \times \frac{\partial u'}{\partial x}|_{t+dt} > \\
&=< \widehat{\frac{\partial u'}{\partial x}}|_{t} \times \widehat{\frac{\partial u'}{\partial x}}|_{t+dt} > + < \beta_t \times \widehat{\frac{\partial u'}{\partial x}}|_{t+dt} > + \widehat{\frac{\partial u'}{\partial x}}|_{t} \times \beta_{t+dt} > + < \beta_t \times \beta_{t+dt} > \\
&=< \widehat{\frac{\partial u'}{\partial x}}|_{t} \times \widehat{\frac{\partial u'}{\partial x}}|_{t+dt} > \\
&\approx< \widehat{\frac{\partial u'}{\partial x}}|_{t} \times \widehat{\frac{\partial u'}{\partial x}}|_{t} >
\end{aligned}
\tag{1.4}
$$

where β_t and β_{t+dt} are uncorrelated because the new particles entering the interrogation window (IW) at t +dt change the peak shape, so the peak fit random noise is then completely different. This method is valid if dt (the time increment between two velocity fields) is small enough so that the denoised quantities do not change significantly between two time steps but not too small (otherwise there would be no new particles inside the IW). In the experiments carried out, dt is chosen to have time resolved results which means the particle displacement between two frames is less than 10 pixels. The PIV processing (final pass) is done with a window size of 32 pixels $\times$ 32 pixels so that there is already a spatial filtering of the data. Therefore, the filtering introduced by shifting the two derivatives by a maximum of 10 pixels is comparable or smaller than the already existing PIV filtering so that the results should not change significantly. Therefore, this method can be used to denoise experimental data without losing too much information of the true signal. This method might however slightly underestimate the dissipation. The same procedure can also be used in space by selecting different points in the derivative, i.e. multiplying the derivative at x and at x+dx computed with a centred scheme, where dx is the vector spacing. As a 62% overlap is used, the four points used are separated by 36px which corresponds to a second filter which has about the same filter size as the IW.

The denoising process is tested both in space and in time to check the results consistency (table 1). The results are close so that the method seems to be reliable. There is a significant dissipation decrease associated to the denoising process (around a factor 2). These results seems to be consistent because the mixer PIV measurements are expected to be more noisy than

	F (Hz)	$< \overline{\epsilon'} >$ (with noise)	$\widehat{< \overline{\epsilon'} >}$ (space method)	$\widehat{< \overline{\epsilon'} >}$ (time method)	$\widehat{< \overline{\epsilon'_\tau} >}$ (time method)
Rectangular blades	1	5.2E-03	3.5E-03	3.6E-03	3.7E-03
Rectangular blades	1.5	1.7E-02	1.1E-02	1.2E-02	1.3E-02
Fractal blades	1	4.2E-03	2.6E-03	2.4E-03	2.5E-03
Fractal blades	1.5	1.3E-02	8.2E-03	8.2E-03	8.6E-03

Table 1: Dissipation computation (m^2/s^3)

typical air experiments. Indeed, this noise is amplified by the remaining presence of small air bubbles in water and the difficulty to obtain the optimal particle concentration linked to this high magnification measurement. These results underline also the importance to denoise dissipation. The energy spectrums and two-point statistics do not need to have the same denoising process because the noise is known to be present only at small scales. Therefore, only the small scale part of the results (large k in Fourier space or small r in two-point space) are contaminated by this PIV noise. Eventually, the PIV resolution affects significantly the dissipation results and a small underestimation is expected in our results.

Overall, the dissipation computation is a difficult problem where resolution, noise and convergence affect significantly the results. For these experiments, the resolution is acceptable in several configurations which can be used for reference, the noise impact is removed through denoising process and the convergence is achieved through an averaging over 100,000 velocity fields (corresponding to 50,000 uncorrelated) and space averaging over the field of view. The dissipation estimate is expected to be slightly underestimated. For simplicity the notation $\widehat{(.)}$ is not used in the publication but all the dissipation results are denoised.

1.2. *Taylor micro scale and Taylor Reynolds number*

The following formulation of the Taylor micro-scale is used:

$$\lambda = \sqrt{\frac{15\nu}{\epsilon}}\sqrt{\frac{u_x'^2 + u_z'^2}{2}} \tag{1.5}$$

The value of the Taylor scale can vary significantly with the formulation choice. However, the variation from one configuration to the other should remain consistent whatever the formulation. The following formulation is also tested:

$$\widetilde{\lambda} = \sqrt{\frac{15\nu}{\epsilon}}\sqrt{\frac{2u_x'^2 + u_z'^2}{3}} \tag{1.6}$$

This formulation overestimates the value by a close to constant proportion between 20% and 25% compared to 1.5. The plots collapse is nearly unchanged when this later estimate is used to non-dimensionalize r.

The Reynolds number based on the Taylor length is calculated:

$$Re_\lambda = \frac{\lambda\sqrt{u_x'^2 + u_z'^2}}{\nu} \tag{1.7}$$

This number is used to quantify the turbulence development. The following formulation is also tested:

$$\widetilde{Re_\lambda} = \frac{\widetilde{\lambda}\sqrt{2u_x'^2 + u_z'^2}}{\nu} \tag{1.8}$$

This formulation overestimates the value by a close to constant proportion between 45% and 55% compared to 1.7. This magnitude difference is significant but the main risk is to overestimate the Reynolds number. Therefore, the formulation with the smallest values is retained.

2. Production and linear transport

2.1. *Two-point turbulence production rate results*

In this section we present results on the truncated and surrogate two-point production estimates introduced in Beaumard *et al.* (2024).

We calculate space averages over the field of view of the four truncated and the four surrogate two-point production rates in the eight equations above. In figures 1, 2, 3 and 4 we plot, versus $r_1 \equiv r_x$ and $r_3 \equiv r_z$, the four average surrogate two-point production rates $\langle\widetilde{\widetilde{P_r}}\rangle$, $\langle\widetilde{\widetilde{P^l_{Xr}}}\rangle$, $\langle\widetilde{\widetilde{P_X}}\rangle$ and $\langle\widetilde{\widetilde{P^l_{Xr}}}\rangle$ where the brackets signify space-averaging. We plot them normalised by $\frac{\langle\overline{\epsilon'}\rangle}{2}$ where $\epsilon' \equiv \nu\frac{\partial u_i'}{\partial\zeta_j}\frac{\partial u_i'}{\partial\zeta_j}$ is estimated on the basis of our 2D2C PIV data using its axisymmetric formulation (see subsection 1.1 where we also report that we did not find very significant differences in the values of $\langle\overline{\epsilon'}\rangle$ calculated either on the basis of small-scale axisymmetry or on the basis of small-scale isotropy). $\frac{\langle\overline{\epsilon'}\rangle}{2}$ is used to non-dimensionalize results instead of $\langle\overline{\epsilon'}\rangle$ because the turbulence dissipation term in equation (2.4) in Beaumard *et al.* (2024), once averaged in space, is $< \frac{\nu}{4}\overline{\frac{\partial u_i'^+}{\partial\zeta_k^+}\frac{\partial u_i'^+}{\partial\zeta_k^+}} + \frac{\nu}{4}\overline{\frac{\partial u_i'^-}{\partial\zeta_k^-}\frac{\partial u_i'^-}{\partial\zeta_k^-}} > \approx \frac{1}{2} < \epsilon' >$.

In the plots in figures 1 and 2, $\langle\widetilde{\widetilde{P_r}}\rangle$ is relatively small and $\langle\widetilde{\widetilde{P^s_{Xr}}}\rangle$ is negligible, irrespective of experimental configuration, for most values of r_x and r_z that our field of view allows us to access. Plots, not shown here for economy of space, of the corresponding truncations $\langle\widetilde{P_r}\rangle$ and $\langle\widetilde{P^s_{Xr}}\rangle$ are very similar. The largest absolute values of $\langle\widetilde{\widetilde{P_r}}\rangle$ are obtained at relatively large scales $r_z = 5\lambda \approx R/5$ with values around $0.15\frac{\langle\overline{\epsilon'}\rangle}{2}$ which is not negligible but still relatively small. These values decrease with decreasing two-point separation lengths as $\langle\widetilde{\widetilde{P_r}}\rangle$ tends to zero when $\boldsymbol{r}$ tends to zero. Furthermore, the increase of $\langle\widetilde{\widetilde{P_r}}\rangle$ with increasing two-point separation is also much smaller than the increase of two-point turbulence production in the intermediate layer of fully developed turbulent channel flow found by Apostolidis *et al.* (2023).

Looking at figure 4, we can hypothesise that cross-scale two-point production is negligible in the large-scale energy equation (2.8) in Beaumard *et al.* (2024), and a similar conclusion arises from respective plots of the average surrogate $\langle\widetilde{P^l_{Xr}}\rangle$ (not shown given the very close resemblance with figure 4). However, unlike $\langle\widetilde{\widetilde{P_r}}\rangle$, $\langle\widetilde{P_r}\rangle$, $\langle\widetilde{\widetilde{P^l_{Xr}}}\rangle$, $\langle\widetilde{P^l_{Xr}}\rangle$, $\langle\widetilde{\widetilde{P^l_{Xr}}}\rangle$ and $\langle\widetilde{P^l_{Xr}}\rangle$ which are all close to zero over a wide range of scales r_x and r_z for all four experimental configurations, $\langle\widetilde{\widetilde{P_X}}\rangle$ and $\langle\widetilde{P_X}\rangle$ do not decrease towards 0 with decreasing two-point separation and can even be comparable to $\frac{\langle\overline{\epsilon'}\rangle}{2}$ at the very smallest separations. Figure 3 shows this clearly for $\langle\widetilde{\widetilde{P_X}}\rangle$ and the corresponding plots (not shown here) for $\langle\widetilde{P_X}\rangle$ are qualitatively similar but with different quantitative values. In particular, $\langle\widetilde{\widetilde{P_X}}\rangle$ and $\langle\widetilde{P_X}\rangle$ do not tend to zero as $\mathbf{r}$ tends to 0 in agreement with the point made in Beaumard *et al.* (2024) that P_X tends to $-\overline{u_j'u_i'}\Sigma_{ij}$ in the limit $\mathbf{r} \to \mathbf{0}$ and therefore does

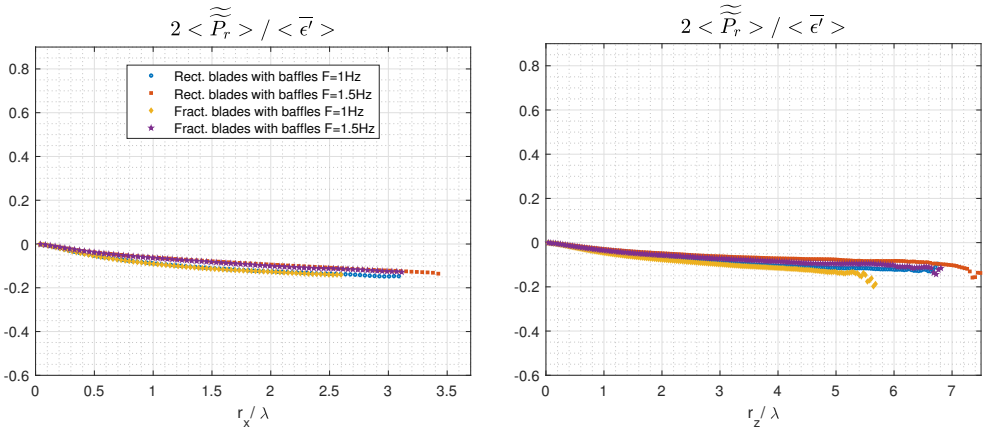

(a) r_x direction (b) r_z direction

Figure 1: Production surrogate defined in equation (5.2) in Beaumard *et al.* (2024) along two radial directions

not tend to zero if there is non-vanishing one-point turbulence production present in the flow. However, the ratios $2\langle\widetilde{\widetilde{P_X}}\rangle/\langle\overline{\epsilon'}\rangle$ and $2\langle\widetilde{P_X}\rangle/\langle\overline{\epsilon'}\rangle$ differ between configurations, and in particular for different types of blade, suggesting that there are non-homogeneity differences between the four configurations considered here. In spite of these differences, $\langle\widetilde{\widetilde{P_X}}\rangle$ and $\langle\widetilde{P_X}\rangle$ are typically negative in all configurations suggesting that energy is transferred from the fluctuations to the mean.

Overall, our data support the hypothesis expressed in section 3 in Beaumard *et al.* (2024) that, for the turbulent flows considered here and for scales small enough compared to the large scales of the flow, two-point production P^s_{Xr} may be neglected in the small-scale energy equation (2.4) in Beaumard *et al.* (2024). However, P_r, while smaller than all other terms, may not be convincingly negligible in that equation. In the intermediate layer of fully developed turbulent channel flow, P_r was also found by Apostolidis *et al.* (2023) not to be negligible at scales comparable to and larger than the Taylor length, but the ratio of P_r to turbulence dissipation rate was significantly higher than in the present flow.

2.2. *Small scale linear transport results*

In this section we evaluate in our flow the two terms in the small scale linear transport $(\overline{\boldsymbol{u_X}}.\boldsymbol{\nabla_X} + \boldsymbol{\delta\overline{u}}.\boldsymbol{\nabla_r})\,\frac{1}{2}\overline{|\boldsymbol{\delta u'}|^2}$. With our 2D2C PIV data, we can only consider a truncation and a surrogate estimate. The truncation is $\left(\overline{u_{Xx}}\frac{\partial}{\partial X_x} + \overline{u_{Xz}}\frac{\partial}{\partial X_z} + \delta\overline{u}_x\frac{\partial}{\partial r_x} + \delta\overline{u}_z\frac{\partial}{\partial r_z}\right)\frac{1}{2}\left(\overline{\delta u_x'^2 + \delta u_z'^2}\right)$ and the surrogate estimate is obtained by making the assumptions $\overline{\delta u_x'^2} = \overline{\delta u_y'^2}$, $\overline{u_{Xx}\frac{\partial}{\partial X_x}\frac{1}{2}|\boldsymbol{\delta u'}|^2} = \overline{u_{Xy}\frac{\partial}{\partial X_y}\frac{1}{2}|\boldsymbol{\delta u'}|^2}$ and $\delta\overline{u}_x\frac{\partial}{\partial r_x}\frac{1}{2}\overline{|\boldsymbol{\delta u'}|^2} = \delta\overline{u}_y\frac{\partial}{\partial r_y}\frac{1}{2}\overline{|\boldsymbol{\delta u'}|^2}$. Our surrogate estimate of $(\overline{\boldsymbol{u_X}}.\boldsymbol{\nabla_X} + \boldsymbol{\delta\overline{u}}.\boldsymbol{\nabla_r})\,\frac{1}{2}\overline{|\boldsymbol{\delta u'}|^2}$ is therefore $\left(2\overline{u_{Xx}}\frac{\partial}{\partial X_x} + \overline{u_{Xz}}\frac{\partial}{\partial X_z} + 2\delta\overline{u}_x\frac{\partial}{\partial r_x} + \delta\overline{u}_z\frac{\partial}{\partial r_z}\right)\frac{1}{2}\left(\overline{2\delta u_x'^2 + \delta u_z'^2}\right)$.

We calculate space-averages of the truncation and the surrogate estimate in two parts: i.e. $\langle\left(\overline{u_{Xx}}\frac{\partial}{\partial X_x} + \overline{u_{Xz}}\frac{\partial}{\partial X_z}\right)\frac{1}{2}\left(\overline{\delta u_x'^2 + \delta u_z'^2}\right)\rangle$ and $\langle\left(\delta\overline{u}_x\frac{\partial}{\partial r_x} + \delta\overline{u}_z\frac{\partial}{\partial r_z}\right)\frac{1}{2}\left(\overline{\delta u_x'^2 + \delta u_z'^2}\right)\rangle$ for the truncation, and for the surrogate estimate $\langle\left(2\overline{u_{Xx}}\frac{\partial}{\partial X_x} + \overline{u_{Xz}}\frac{\partial}{\partial X_z}\right)\frac{1}{2}\left(\overline{2\delta u_x'^2 + \delta u_z'^2}\right)\rangle$ and $\langle\left(2\delta\overline{u}_x\frac{\partial}{\partial r_x} + \delta\overline{u}_z\frac{\partial}{\partial r_z}\right)\frac{1}{2}\left(\overline{2\delta u_x'^2 + \delta u_z'^2}\right)\rangle$. Both parts of the space-average truncation and of the

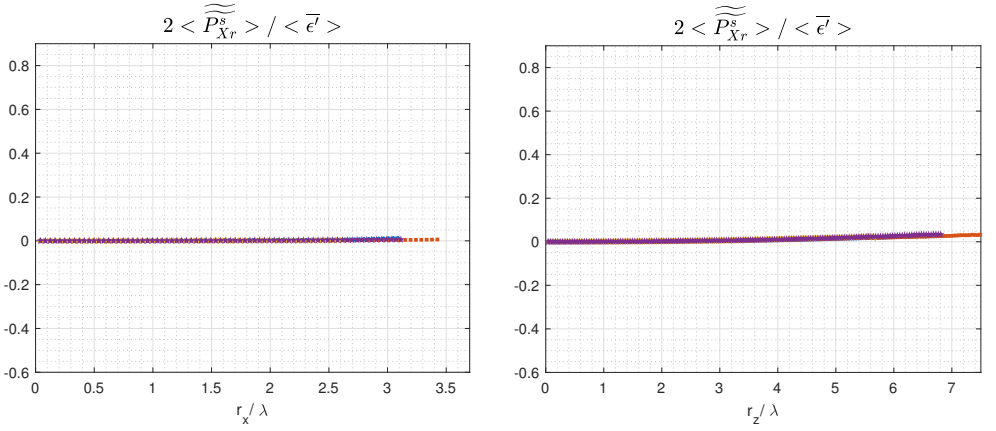

(a) r_x direction (b) r_z direction

Figure 2: Production surrogate defined in equation (5.4) in Beaumard *et al.* (2024) along two radial directions

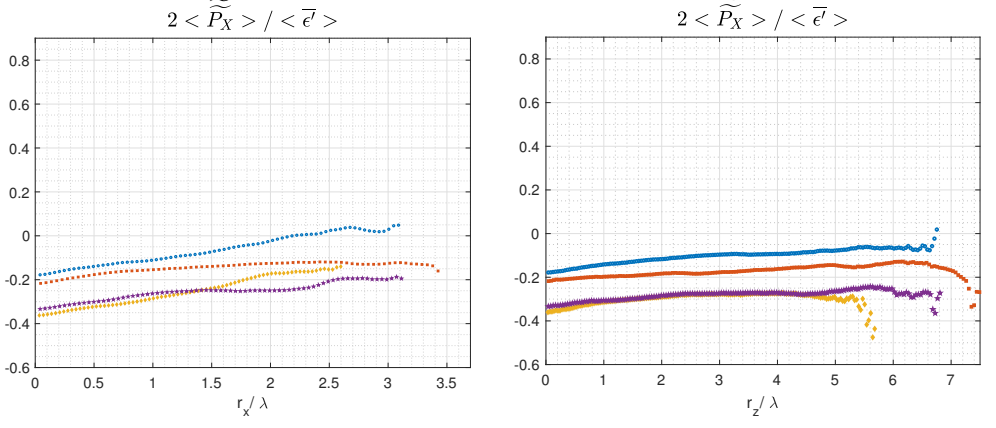

(a) r_x direction (b) r_z direction

Figure 3: Production surrogate defined in equation (5.6) in Beaumard *et al.* (2024) along two radial directions

space-average surrogate are relatively small compared to $\langle\overline{\epsilon'}\rangle/2$ over a significant range of scales in all four configurations, increasing slowly in magnitude with increasing $|\boldsymbol{r}|$ and reaching at $r_z = 6.8\lambda \approx 0.3R$ a value of $0.23\langle\overline{\epsilon'}\rangle/2$ for the conservative surrogate estimate and of $0.14\langle\overline{\epsilon'}\rangle/2$ for the truncation. In figures 5a, 5b, 6a and 6b we plot the two space-average surrogate parts normalised by $\langle\overline{\epsilon'}\rangle/2$ versus r_x and r_z.

There are therefore grounds to neglect some but not all of the terms in $(\overline{\boldsymbol{u_X}}.\boldsymbol{\nabla_X} + \boldsymbol{\delta\overline{u}}.\boldsymbol{\nabla_r})\ \frac{1}{2}\overline{|\boldsymbol{\delta u'}|^2}$ from the small-scale energy equation (2.4) in Beaumard *et al.* (2024) at small enough scales.

3. Peak locking quantification and impact on turbulence results

In this section, we quantify the peak-locking present in our measurements and its impact on the results.

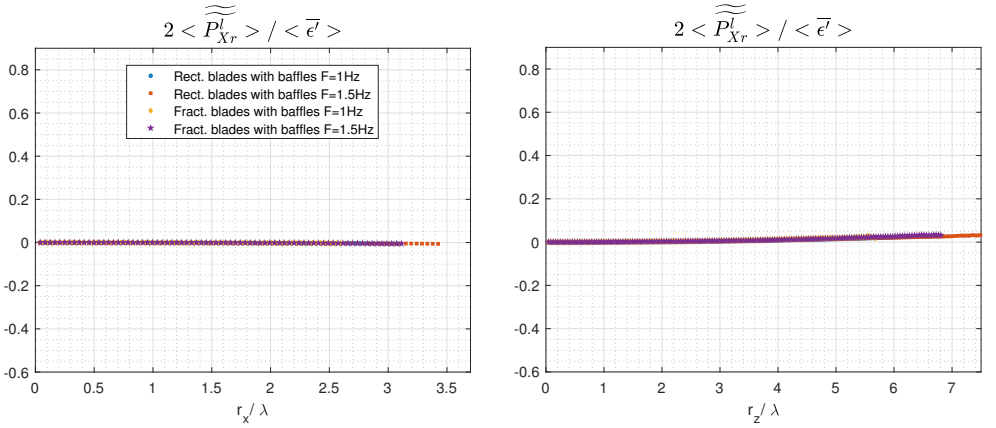

(a) r_x direction (b) r_z direction

Figure 4: Production surrogate defined in equation (5.8) in Beaumard *et al.* (2024) along two radial directions

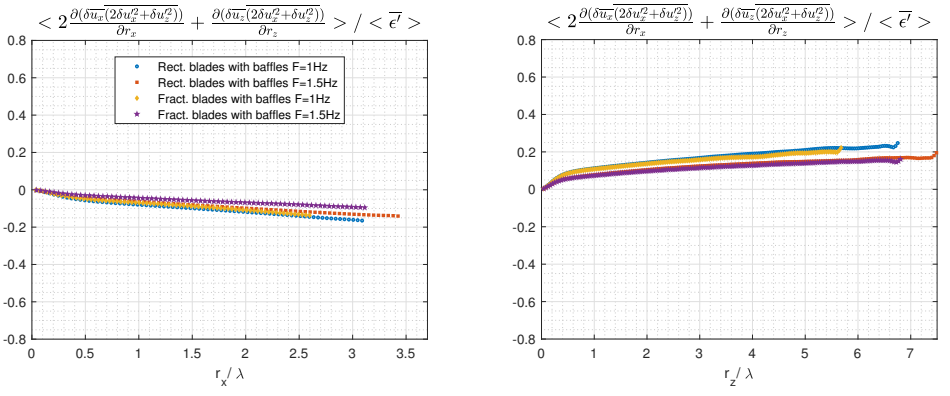

(a) r_x direction (b) r_z direction

Figure 5: Surrogate of rate of linear transport in scales in equation (2.4) in Beaumard *et al.* (2024)

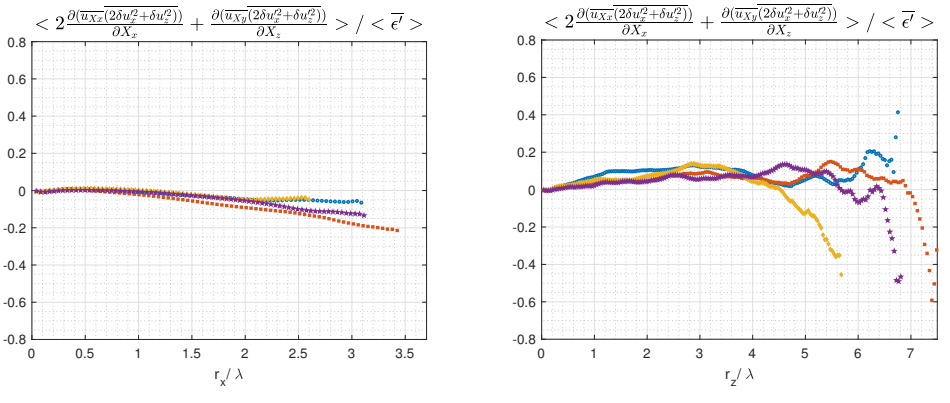

(a) r_x direction (b) r_z direction

Figure 6: Surrogate of rate of linear transport in space in equation (2.4) in Beaumard *et al.* (2024)

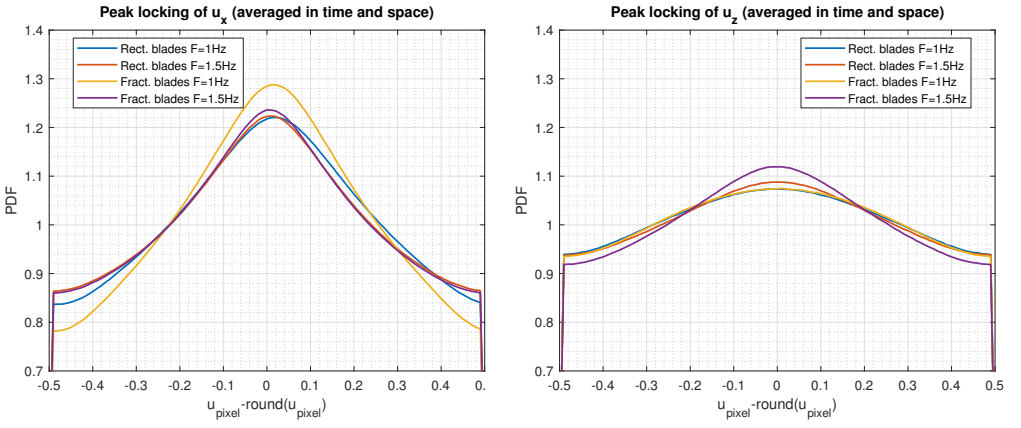

(a) u_x decimal part (b) u_z decimal part

Figure 7: Probability distribution function of the decimal part

3.1. *Peak locking quantification*

The experimental PIV measurements introduce a random error which respect a Gaussian distribution law. This distribution law has a zero mean and usually a standard deviation around 0.1 - 0.2 px (Raffel *et al.* (2018)). It introduces also the peak locking systematic error as explained previously. This latter error can be quantified through the probability distribution function (PDF) of the particle displacement in pixel: $u_{pixel} - round(u_{pixel})$. A constant PDF means there is no peak locking. The results are presented in figure 7. Some peak-locking is observed in the results. This error is similar for all configurations and is more important in the x direction.

The peak locking error can be modeled as $-a.sin(2\pi(u_{true}-round(u_{true}))$ so that $u_{measured} = u_{true} - a.sin(2\pi(u_{true} - round(u_{true})) + \epsilon_{Gaussian}$, where $\epsilon_{Gaussian}$ is the random noise and u_{true} the true displacement with IW filtering effect. However, the peak locking can be estimated as $a.sin(2\pi(u_{measured} - round(u_{measured}))$ according to Cholemari (2007). The coefficient represents the peak-locking magnitude and it can be evaluated from experimental data using the previous approximation. A correction is added to the contaminated data until the PDF of the rounded part of the displacement is nearly flat. The coefficient a used for this correction gives a good estimate of the peak locking magnitude. For all configurations, the maximal value of a is estimated to be $0.02px$.
It means the peak locking error order of magnitude is around 10 times smaller than the Gaussian PIV noise. However, this error does not necessarily disappear when averaged because it is a systematic error. This is why the consequences of this phenomenon on the results of this study are quantified.

3.2. *Peak locking impact on spatial energy spectrums*

The peak locking impact on spatial energy spectrums is evaluated by introducing artificial peak locking into Direct Numerical Simulations (DNS).

The DNS dataset was computed by Jean-Philippe Laval from LMFL. It is a $512 \times 512 \times 512$ pseudo-spectral periodic simulation with $Re_\lambda \approx 140$. The resolution is around 1.6η. The energy spectrum is computed directly from the simulation results and from the results affected by a modeled peak locking:

$$u_{peaklocking} = u_{simulation} - a \times sin(2\pi(u_{simulation} - round(u_{simulation})) \qquad (3.1)$$

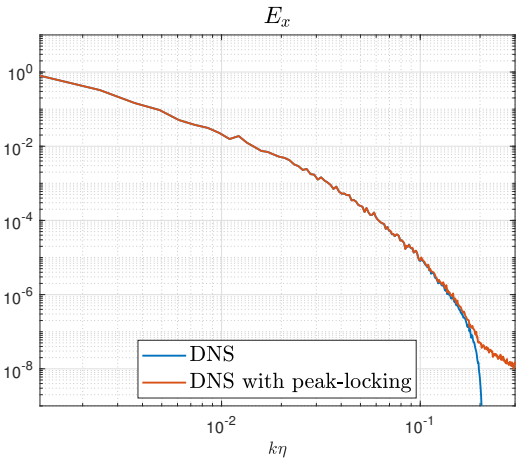

Figure 8: Peak locking impact on spatial energy spectrum from DNS.

with $a = 0.02px$.

The results are presented in figure 8. The peak-locking does not have any consequence on the spatial energy spectrum except at the very high wavelengths where in reality it will be much more polluted by the PIV noise. Therefore, the experimental results can be used to compute energy spectrums without restrictions.

3.3. *Peak-locking impact on two-point statistics*

The peak locking impact on averaged two-point statistics is quantified by introducing a peak locking correction in the experimental data. Then, we evaluate the results evolution after the correction. The correction defined in Cholemari (2007) is used:

$$u_{corrected} = u_{measured} + a_{estimated} \times sin(2\pi(u_{measured} - round(u_{measured})) \tag{3.2}$$

where a is estimated for each configuration in x and y direction.

The results are presented in figure 9. No difference is observed between the results with and without peak locking correction. Therefore, the experimental results can be used to compute two-point statistics without restrictions. The results presented in the publication do not contain peak locking correction.

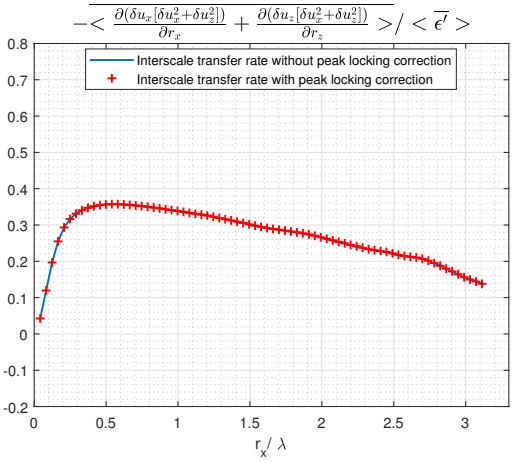

Figure 9: Peak-locking impact on energy interscale transfer rate

4. Space averaging impact on results

Structure functions are averaged in space to improve convergence as the results collapse is very sensitive to convergence. Therefore, the results are plotted in figure 10a, 10b, 10c and 10d without space averaging to check it does not affect results. Only one configuration is presented but it is representative of the four configurations. $V_I = V_O.R_O^{-1/4}$ and $l_I = l_O.R_O^{-3/4}$ are defined arbitrarily where $l_O = D$ and $V_O = \sqrt{\overline{u_x'^2} + \overline{u_z'^2}}$. However, it is important to note that V_I and l_I are nearly constant over the spatial domain with a variation of less than 3% for the two quantities. The error bars for these results are computed with classical convergence formula. The largest error bar of all positions is used and centered on the spatially averaged structure function (in red). The results collapse within error bars for $\overline{\delta u_x'^2}/V_I^2 = f(r_x)$, $\overline{\delta u_x'^2}/V_I^2 = f(r_z)$, $\overline{\delta u_z'^2}/V_I^2 = f(r_x)$ and $\overline{\delta u_z'^2}/V_I^2 = f(r_z)$, which confirms that space averaging does not distort the results and can be therefore used to improve convergence. These results are also consistent with the inner region structure functions' similarity assumed in equation (7.2) in Beaumard *et al.* (2024). The outer region is not accessible with our dataset.

Third order statistics are even more difficult to converge than second order statistics. Therefore, space averaging is mandatory to converge results. The most critical quantity is the interspace transport as it is computed with space derivatives which can be affected by space averaging. The interspace transport averaged in time and space is compared to the same quantity averaged in time and in space for only one direction (z) but at different x locations (figure 11). The results are not well converged due to the number of points reduction. The shape of the non-converged functions at the different x positions seems to be consistent with the converged results averaged in space. Therefore, spatial averaging can be used to improve the results convergence without loss of information and without significant distortion of the results.

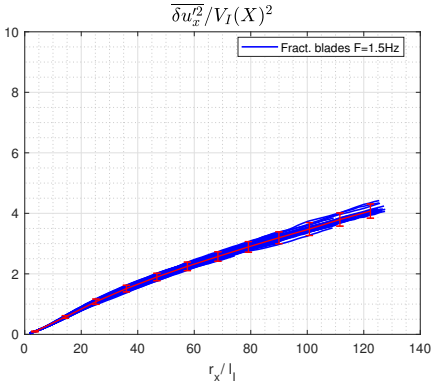

(a) Time averaged results of $\overline{\delta u_x'^2}/V_I^2$ in r_x direction at different spatial positions.
In red: $< \overline{\delta u_x'^2}/V_I^2 >$

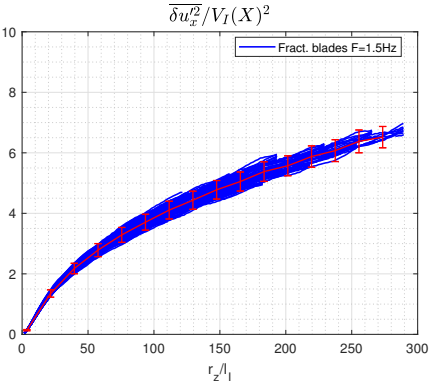

(b) Time averaged results of $\overline{\delta u_x'^2}/V_I^2$ in r_z direction at different spatial positions.
In red: $< \overline{\delta u_x'^2}/V_I^2 >$

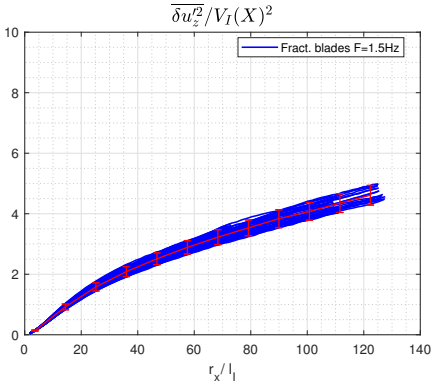

(c) Time averaged results of $\overline{\delta u_z'^2}/V_I^2$ in r_x direction at different spatial positions.
In red: $< \overline{\delta u_z'^2}/V_I^2 >$

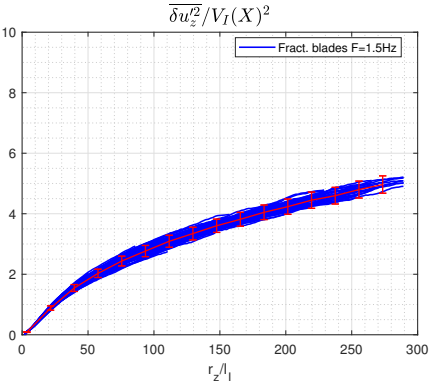

(d) Time averaged results of $\overline{\delta u_z'^2}/V_I^2$ in r_z direction at different spatial positions.
In red: $< \overline{\delta u_z'^2}/V_I^2 >$

Figure 10: Time averaged structure functions at different spatial locations

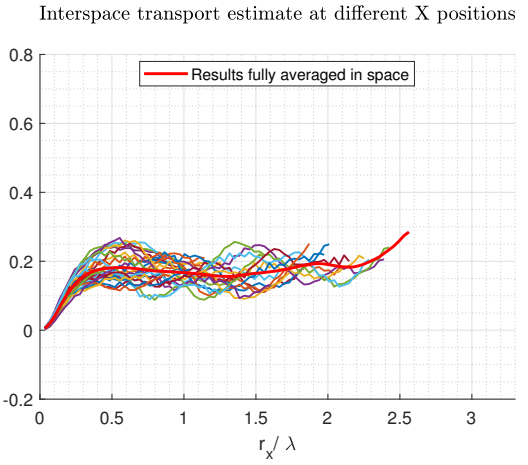

Figure 11: Space averaging impact on interspace transport

REFERENCES

Apostolidis, A, Laval, J P & Vassilicos, J C 2023 Turbulent cascade in fully developed 2 turbulent channel flow. *Journal of Fluid Mechanics* .

Beaumard, P, Bragança, P, Cuvier, C, Steiros, K & Vassilicos, J C 2024 Scale-by-scale non-equilibrium with Kolmogorov-like scalings in non-homogeneous stationary turbulence. *Journal of Fluid Mechanics* .

Cholemari, Murali R. 2007 Modeling and correction of peak-locking in digital PIV. *Experiments in Fluids* **42** (6), 913–922.

Foucaut, Jean Marc, George, William K., Stanislas, Michel & Cuvier, Christophe 2021 Optimization of a SPIV experiment for derivative moments assessment in a turbulent boundary layer. *Experiments in Fluids* **62** (12), 244.

George, William K. & Hussein, Hussein J. 1991 Locally axisymmetric turbulence. *Journal of Fluid Mechanics* **233**, 1–23, publisher: Cambridge University Press.

Raffel, Markus, Willert, Christian E., Scarano, Fulvio, Kähler, Christian J., Wereley, Steve T. & Kompenhans, Jürgen 2018 *Particle Image Velocimetry: A Practical Guide*. Cham: Springer International Publishing.